THE JOURNAL OF BIOLOGICAL CHEMISTRY
Vol. 278, No. 4, Issue of January 24, pp. 2490–2502, 2003
Printed in U.S.A.

Synergistic Anion and Metal Binding to the Ferric Ion-binding Protein from *Neisseria gonorrhoeae**[S]

Received for publication, August 27, 2002
Published, JBC Papers in Press, October 7, 2002, DOI 10.1074/jbc.M208776200

Maolin Guo‡§, Ian Harvey¶, Weiping Yang‡§, Lorraine Coghill‡, Dominic J. Campopiano‡, John A. Parkinson‡, Ross T. A. MacGillivray‖, Wesley R. Harris, and Peter J. Sadler‡ ‡‡**

*From the ‡School of Chemistry, University of Edinburgh, Edinburgh EH9 3JJ, United Kingdom, ¶Synchrotron Radiation Department, CLRC Daresbury Laboratory, Warrington WA4 4AD, United Kingdom, ‖Department of Biochemistry and Molecular Biology, University of British Columbia, Vancouver, British Columbia V6T 1Z3, Canada, and **Department of Chemistry, University of Missouri, St. Louis, Missouri 63121*

The 34-kDa periplasmic iron-transport protein (FBP) from *Neisseria gonorrhoeae* (nFBP) contains Fe(III) and (hydrogen)phosphate (synergistic anion). It has a characteristic ligand-to-metal charge-transfer absorption band at 481 nm. Phosphate can be displaced by (bi)carbonate to give Fe·CO_3·nFBP (λ_{max} 459 nm). The local structures of native Fe-PO_4-nFBP and Fe·CO_3·nFBP were determined by EXAFS at the FeK edge using full multiple scattering analysis. The EXAFS analysis reveals that both phosphate and carbonate ligands bind to FBP in monodentate mode in contrast to transferrins, which bind carbonate in bidentate mode. The EXAFS analysis also suggests an alternative to the crystallographically determined position of the Glu ligand, and this in turn suggests that an H-bonding network may help to stabilize monodentate binding of the synergistic anion. The anions oxalate, pyrophosphate, and nitrilotriacetate also appear to serve as synergistic anions but not sulfate or perchlorate. The oxidation of Fe(II) in the presence of nFBP led to a weak Fe(III)·nFBP complex (λ_{max} 471 nm). Iron and phosphate can be removed from FBP at low pH (pH 4.5) in the presence of a large excess of citrate. Apo-FBP is less soluble and less stable than Fe·nFBP and binds relatively weakly to Ga(III) and Bi(III) but not to Co(III) ions, all of which bind strongly to apo-human serum transferrin.

Iron is an essential nutrient absolutely required for all organisms with the possible exception of *Lactobacillus* and *Borrelia burgdorferi* (1, 2). Iron is abundant in the environment but tends to precipitate as ferric hydroxide under aerobic aqueous conditions at neutral pH where the concentration of free Fe(III) is 10^{-18} M, 12 orders of magnitude lower than that required for bacterial growth (3, 4). In humans and other mammals, iron is sequestered and transported by transferrins and lactoferrins and stored in ferritin (5). The tight binding of iron by these proteins leads to a very low level of free iron in the host, which acts as an antibacterial defense mechanism. However, some pathogenic bacteria, such as *Neisseria meningitidis*, *N. gonorrhoeae*, *Haemophilus influenzae*, *Actinobacillus actinomycetemcomitans*, *and Pasteurella hemolytica*, have developed highly efficient iron-uptake systems including specific iron-binding proteins (FBPs)[1] to sequester iron from hosts (6, 7). Iron is transported in the periplasm of these pathogens by FBP, which is a highly conserved periplasmic protein required for virulence (7–12). Therefore, structural studies of FBP are important for understanding the iron-uptake mechanism in these pathogens and could aid the design of novel bacteriostatic agents targeted on this protein.

FBP has been called "bacterial transferrin" because of its remarkable similarity to transferrin. A recent crystal structure of FBP from *H. influenzae* (hFBP) has revealed that it is structurally homologous to one lobe of transferrin but without sequence homology (9). The Fe(III) binding site in hFBP resembles the two Fe(III) binding sites in transferrin containing two *cis*-Tyr ligands and one His ligand but with Glu instead of the Asp residue found in transferrins (see Structure I). A striking difference is that hFBP appears to have a monodentate tetrahedral phosphate (or hydrogen phosphate) bound to Fe(III) as the synergistic anion together with a water ligand (9), whereas transferrins use bidentate (bi)carbonate as the synergistic anion. Transferrin can use other carboxylates as synergistic anions but cannot use phosphate or sulfate (13). The synergistic anion binding properties of transferrins including their role in metal binding and release have been well documented (14–16), but only recently have the synergistic anion binding properties of bacterial FBP been investigated (9, 17). The FBP from *N. gonorrhoeae* (nFBP) has been biochemically characterized (18) and subsequently expressed in *Escherichia coli* (19, 20). It has been reported that a large excess of $NaHCO_3$ increases the iron binding capacity of apo-FBP (21).

We have investigated the binding of anions and metal ions to recombinant FBP from *N. gonorrhoeae* by a variety of techniques including UV-visible spectroscopy, inductively coupled plasma atomic emission spectrometry (ICP-AES), electrospray mass spectrometry, multinuclear NMR spectroscopy, and EX-

* This work was supported in part by an Overseas Research Scholar award from the Committee of Vice-Chancellors and Principals, a scholarship (to M. G.) from the University of Edinburgh, and Showcase and Joint Infrastructure Fund awards from The Wellcome Trust (Edinburgh Protein Interaction Centre). The costs of publication of this article were defrayed in part by the payment of page charges. This article must therefore be hereby marked "*advertisement*" in accordance with 18 U.S.C. Section 1734 solely to indicate this fact.

[S] The on-line version of this article (available at *http://www.jbc.org*) contains Figs. S1–S7.

§ Present address: Dept. of Molecular Biology and Biochemistry, University of California, Irvine, CA 92697.

‡‡ To whom correspondence should be addressed. Tel.: 44-131-650-4729; Fax: 44-131-650-6452; E-mail: p.j.sadler@ed.ac.uk.

[1] The abbreviations used are: FBP, ferric ion-binding protein; nFBP, ferric ion-binding protein from *N. gonorrhoeae*; hFBP, ferric ion-binding protein from *Haemophilus influenzae*; EXAFS, extended x-ray absorption fine structure; TF, transferrin; hTF, human serum transferrin; CTAB, cetyltrimethylammonium bromide; H_3NTA, nitrilotriacetic acid; ICP-AES, inductively coupled plasma atomic emission spectrometry; XANES, x-ray absorption near edge structure; Fe-EHPG, *N*,*N*′-ethylene-bis(*o*-hydroxyphenylglycine)-iron(III); LMCT, ligand-to-metal charge-transfer.

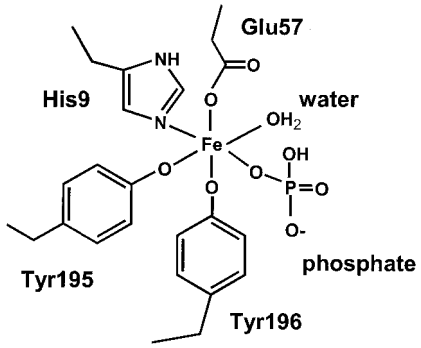

STRUCTURE 1. **Fe(III) binding site in FBP.** The state of protonation of phosphate is unknown.

AFS. EXAFS is a technique capable of providing, in principle, metal-ligand bond lengths to the same accuracy as a small molecule crystal structure (≤0.02 Å). In the case of metalloproteins, this accuracy significantly exceeds the accuracy obtained from all but atomic resolution (<1.2 Å) crystal structures. However, this accuracy has not been routinely achieved because of limitations in theory and difficulty with the required calculations. Also, there is a limit to which similar bond lengths can be resolved, which is dependent on the data range and is typically of the order of 0.1 Å. Significant improvements in EXAFS data analysis have occurred in recent years including the use of constrained and restrained refinement (22–25), mapping techniques (25, 26), use of three-dimensional crystal structure coordinates (27–29), and full (*i.e.* including interligand as well as intraligand) multiple scattering (30, 31). These methods have been combined in the analysis program *EXCURV98* (32) and have recently been applied to the copper protein azurin (33) where it gave rise to a significant improvement in the quality of the final simulation and model. We apply these methods here to both the $(H)PO_4$ and $(H)CO_3$ adducts of Fe·nFBP. These studies are important for understanding the mechanisms for iron transport in this pathogenic bacterium.

EXPERIMENTAL PROCEDURES

Materials—Electrophoresis was carried out using a Bio-Rad Protean II Minigel system (protein) and Invitrogen H5 system (DNA). An Amersham Biosciences fast protein liquid chromatography system and columns were used for chromatographic separations of proteins. Precast SDS-PAGE gels (10% bis-Tris) were purchased from Novex and were used according to the manufacturer's instructions.

Monosodium citrate (Aldrich), $NaHCO_3$ (Aldrich), nitrilotriacetic acid (H_3NTA, Aldrich), NaH_2PO_4, and Na_2HPO_4 (BDH), tetrasodium pyrophosphate (Strem), Hepes (Aldrich), Tris (Aldrich), cetyltrimethylammonium bromide (CTAB, Aldrich), and $NaH^{13}CO_3$ (MSD isotopes, >99% enriched) were used as received. Iron, phosphorus, gallium, bismuth, and cobalt atomic absorption standard solutions were purchased from Aldrich. All other chemicals were reagent grade. A freshly prepared physiological buffer was used with final concentrations of 4 mM NaH_2PO_4, 100 mM NaCl, and 25 mM $NaHCO_3$ (pH 7.4).

Stock solutions of $[Fe(III)(NTA)_2]$, $[Ga(III)(NTA)_2]$, and [Bi(III)(NTA)] were prepared from the iron, gallium, and bismuth atomic absorption standard solutions and the stoichiometric amount of H_3NTA. The pH values were raised slowly to ~5.5 with microliter amounts of NaOH (1 M). Diluted solutions were used where necessary. Aqua Co(III) ions are unstable under normal conditions, and so $Na_3Co(III)(CO_3)_3$ was prepared according to published procedures (34, 35). The purity was confirmed by carbon and cobalt analysis. A stock solution of $Na_3Co(III)(CO_3)_3$ was prepared in 1 M $NaHCO_3$ according to published methods (36). This complex has been used successfully to load human transferrin with Co(III) (36).

Overexpression of nFBP—nFBP was overexpressed in *E. coli* Top10 One Shot™ or DH5αF′ cells (Invitrogen) transformed with pTRC99A/FBP. A single colony from freshly transformed cells was used to inoculate 5 ml of 2YT broth (Bacto-tryptone (16 g), Bacto-yeast extract (10 g), NaCl (5 g) dissolved in distilled water (1 liter), and then adjusted to pH 7.5 with NaOH) containing 100 μg/ml ampicillin in a sterile 10-ml vial. This culture was shaken overnight at 310 K and used to inoculate 1 liter of 2YT with 100 μg/ml ampicillin in sterile 500-ml flasks. After the flask was shaken overnight at 310 K, a pink pellet of cells was isolated by centrifugation at 10,000 × *g* for 15 min at 277 K and stored at 253 K.

Purification of nFBP—nFBP was purified by a modification of the method of Berish *et al.* (20). The pink pellet (~5 g) was defrosted at room temperature and resuspended in 50 ml of 1 M Tris (pH 8.0). 50 ml of 2% CTAB then was added followed by stirring slowly overnight at 310 K. The white insoluble material was removed by centrifugation at 10,000 × *g* for 15 min at 277 K. The supernatant (cell-free extract) was diluted to a final volume of 1 liter by adding distilled water and then filtered using Whatman number 4 paper (Fisher). The cell-free extract was applied to a RESOURCE®S cation exchange column (1 or 6 ml, Amersham Biosciences) connected to a fast protein liquid chromatography system, washed according to the manufacturer's instructions, and equilibrated with 10 mM Tris buffer (pH 8.0). The filtered CTAB extract was loaded onto the column at a flow rate of 4 ml/min. Unbound proteins were removed by extensive washing with low salt buffer. Proteins were eluted with a linear NaCl gradient of low-to-high salt (0–1 M NaCl) over 20 column volumes in 10 mM Tris buffer. Pink fractions were collected and were analyzed by SDS-PAGE. nFBP was desalted by dialysis and concentrated by ultrafiltration (Amicon concentrator). The concentration of purified protein was determined by the BCA method using bovine serum albumin as a reference (37).

Preparation of Apo-nFBP—Apo-nFBP was prepared by treatment of holo-nFBP solutions in a Centricon 10 microconcentrator (Amicon) with 250 mM sodium citrate (pH 4.5) at least four times until there was negligible absorbance at 481 nm. The apo-nFBP was then washed four times with 2 ml of 0.1 M KCl. At this point, the colorless protein was exhaustively exchanged into the buffer to be used in different experiments (Centricon 10).

Mass Spectrometry—Electrospray mass spectrometry was performed on a Micromass Platform II quadrupole mass spectrometer equipped with an electrospray ion source. The purified holo-protein or apoprotein samples in 10 mM Hepes (pH 7.2) were diluted with $MeOH/H_2O$ (1:1, v/v) to a final concentration of 20 μM (20 pmol/μl), and CH_3COOH (final concentration 0.5%) was added to the samples before measurement. The final pH of the protein samples was ~3.7. The mass spectrometer was scanned at intervals of 0.1 s, the scans were accumulated, the spectra were combined, and average molecular mass was determined using the MaxEnt and Transform algorithms of massLynx software.

UV-visible Spectroscopy—All of the UV experiments were performed with 1-cm cuvettes on a computer-controlled Shimadzu UV-1000 spectrometer with temperature control at 298 or 310 K. UV-difference spectra after the addition of metal complex to apo-FBP were recorded immediately and at different time intervals. For titration experiments, aliquots of metal complex (0.5–10 μl) were added and the solution was left to equilibrate at 298 K for 30 min. The binding or release of Fe(III) was monitored by the increase or decrease in absorbance at 481 nm.

NMR Spectroscopy—FBP samples were dissolved in 0.1 M KCl in 10% D_2O, 90% H_2O. The pH was adjusted to 7.4 ± 0.1 when necessary using NaOH and HCl (0.1 M). The pH* values (meter readings) of NMR solutions were recorded before and after NMR measurements.

^1H NMR spectra were recorded on a Bruker DMX 500 spectrometer at 500 MHz, using 0.6 ml of FBP solution (~1 mM) in 5-mm tubes at 298 K using ~1,000 transients, 6-μs (50°) pulses, 1.8-s recycle time, 16,384 data points, and water suppression via presaturation. The chemical shift reference for ^1H was sodium trimethylsilyl-d_4-propionate (TSP). Resolution enhancement of the spectra was achieved by processing the free induction decays with a combination of unshifted sine-bell and exponential functions (line broadening of 1.5–20 Hz) on a Silicon Graphics computer using XWIN-NMR software.

Proton-decoupled ^{31}P NMR spectra were recorded on a Bruker DMX 500 spectrometer operating at 202 MHz. Typically, 3,000–10,000 transients were collected using a pulse-width of 6 μs (50°), relaxation delay of 2 s, and 16,384 data points. The ^{31}P reference was external 85% H_3PO_4. The spectra were processed using exponential functions (line broadening of 2–10 Hz).

Two-dimensional [^1H,^1H], NOESY (mixing time of 100 ms), and TOCSY spectra (mixing time of 50 ms) (38, 39) were acquired on a Bruker DMX 500 spectrometer at 298 K using 4,096 data points in the f2 dimension [^1H], 32–64 increments of t_1, acquisition time of 0.2 s, 96 scans, and 512 increments in the f1 dimension in a total time of ~21 h. Qsine functions were used in both dimensions for processing data using XWIN-NMR 2.0 software. The residual water signal was suppressed by presaturation or pulsed-field gradients. Peaks were referenced to TSP.

ICP-AES—ICP-AES was performed on a Thermo Jarrell Ash IRIS

spectrometer using standard methods. Metal-loaded proteins and apoproteins were purified by using Centricon 10 (Amicon) ultrafilters and washing three times with ultrapure water followed by ultrafiltration after each washing. The final protein solution was diluted with Tris buffer (10 mM).

pH Measurements—The pH values of the solutions were adjusted with HCl or NaOH (DCl or NaOD for samples in D_2O solution) and determined using a Corning 240 pH meter equipped with an Aldrich microcombination electrode calibrated with Aldrich buffer solutions at pH 4, 7, and 10. The pH meter readings for D_2O solutions are recorded as pH* values, *i.e.* uncorrected for the effect of deuterium.

X-ray Absorption Spectroscopy—X-ray spectra were recorded at the iron K edge on EXAFS station 9.3 at Daresbury Laboratory Synchrotron Radiation Source (operating at 2 GeV) using a Si<220> double crystal monochromator and vertically focusing mirror for harmonic rejection. Data for native nFBP and apo-nFBP loaded with Fe(III) in the presence of bicarbonate rather than phosphate were collected at 13 K (using a liquid helium cryostat) in fluorescence mode using a 13-element solid state germanium detector. Data were collected in k space using a k^3-weighted regime for counting time with a total scan time of 40 min. 28 scans were collected from each sample. The edge positions were calibrated against an Fe foil. Samples were prepared as follows. Purified native nFBP was concentrated to 7 mM by ultrafiltration and washed three times with 0.1 M KCl. Fe·CO_3·nFBP (2 mM) was prepared by reacting apo-nFBP with 1.2 mol eq of $Fe(NTA)_2$ in Hepes buffer (pH 7.4) in the presence of 10 mM sodium bicarbonate. The excess of $Fe(NTA)_2$ and free NTA was removed from the yellowish-pink solution by ultrafiltration washing four times with 0.1 M KCl. Data were processed using EXCALIB and SPLINE (modified for use with EXCURV) (40). The EXAFS data were converted into k space. The photoelectron wave vector k is related to the incident photon energy (E) and to the threshold energy (E_o) by Equation 1,

$$k = \sqrt{\frac{2m(E - E_o)}{\hbar^2}} \qquad \text{(Eq. 1)}$$

where m is the mass of an electron. The EXAFS data were analyzed using the fast curved wave (or Rehr-Albers) theory (41) including up to third order multiple scattering contributions in EXCURV98 (32). This version of the program includes interligand scattering terms in the calculations (31). Phase shifts were calculated using Hedin-Lundquist exchange and correlation potentials (42, 43) and tested against the EXAFS data for iron-protoporphyrin IX chloride (chlorohemin) (44) and Fe-EHPG (45). All data analysis was carried out on raw EXAFS data (without Fourier filtering) weighted by k^3 to compensate for diminishing amplitude at high k.

The EXAFS analysis proceeded in a number of stages. (i) Single scattering analysis of the first shell (ligand or nearest neighbor) atoms was the first stage. The Fe-PO_4-nFBP data were then analyzed as follows. (ii) Constrained (rigid body) EXAFS was fit using the crystallographic coordinates of hFBP (1.6 Å resolution, PDB code 1MRP) as starting model. The EXAFS data were simulated retaining the three-dimensional coordinates with full (*i.e.* including interligand in addition to intraligand) multiple scattering. Protein residues were truncated, keeping only those atoms within 5 Å of central iron atom that should be relatively well ordered with respect to iron such as all atoms of the phenolate rings of Tyr-195 and Tyr-196 ($n = 2 \times 7$), all atoms of the imidazole ring of His-9 ($n = 5$), all atoms of the phosphate group ($n = 5$), the terminal part of Glu-57 ($n = 4$) (CG, CD, OE1, OE2), and water ($n = 1$). This gave a total of 29 atoms. Treating each residue as a rigid body means that the position of all the atoms in a multi-atom ligand can be defined using only three parameters: one distance (usually the ligand atom) and two polar angles (θ and φ) while simultaneously maintaining the overdeterminancy of the refinement (see Table III) and maintaining the internal geometry of the residue. (iii) One parameter (Fermi energy) was refined, and Debye-Waller factors were set at values from final simulation. (iv) 13 parameters were refined: Fermi energy, 6 distances for ligand atoms, 5 angles for non-water residues, one single Debye-Waller factor for the 6 six-liganding (nearest neighbor) atoms. It was assumed that the Debye-Waller factors increased with distance from the central atom as it is physically unrealistic to allow more distant non-liganding atoms to have stronger thermal correlations with the metal atom than the nearer atoms (23, 25, 46). Debye-Waller factors were grouped together for similar distances and atom type and scaled to the refined Debye-Waller factor for the ligand atoms. (v) 14 parameters were refined as described above plus a rotation around the vector defined by CG-CD of Glu-57. The starting parameters for the rotation around the CG-CD vector were established by mapping this parameter against the related positional parameters for the Glu-57 ligand. The validity of this methodology was tested using the Fe-EHPG data (see "Results"). (vi) Similar ligand distances ($\delta < 0.1$ Å) were grouped, giving three rather than six ligand distances, and the refinement was repeated. (vii) Restrained refinement against "ideal" bond lengths was derived from the Engh and Huber library (47). A total of 55 two-dimensional 1–2, 1–3, and 1–4 bond length restraints within residues were applied (23). These restraints together with not refining φ values are sufficient to maintain the planarity of the phenolate and imidazole rings. A weighting of EXAFS:restraints of 0.5:0.5 was used. Further details of the procedure used were described previously (for details see Refs. 23, 33, and 46).

Uncertainties were estimated in two ways; 1) by varying a parameter away from its optimal value while optimizing all other parameters until $(D\chi)^2$ (as defined in Equation 1 of Ref. 48) increased by 1 above its minimum value (48) and 2) by calculation of the co-variance matrix. The statistical component of the noise was quantified by subtracting a smooth function obtained from a low pass Fourier filter from the background-subtracted data.

Once a satisfactory simulation of the EXAFS data for Fe-PO_4-nFBP had been obtained, PO_4 was replaced with CO_3 (giving 28 shells), and the analysis was repeated with the Fe·CO_3·nFBP data. After completion of most of the EXAFS analysis, the crystal structure coordinates of nFBP (PDB code 1D9Y) at moderate (2.2 Å) resolution became available (www.rcsb.org).[2] They have been included in the comparisons.

RESULTS

Overexpression and Characterization of nFBP

Cloning and Overexpression of nfbp in E. coli—The vector pTRC99A/FBP was used for the overexpression of the n*fbp* gene. Wild-type nFBP was overexpressed in both Top10 and DH5αF′ *E. coli* cell lines transformed with pTRc99A/FBP. The formation of a pink pellet was indicative of the overexpression of nFBP. Expression levels were similar in 2YT for both cell lines, but Top10 cells containing pTRC99A/FBP gave deeper pink pellets and were used for large scale protein expression. Optimal yields of protein were obtained by aerobic cell growth in 2YT at 310 K for 28–30 h. From a 1-liter cell culture, ~100–200 mg of purified protein was normally obtained.

Purification of nFBP—The overexpressed protein was located in the periplasm of *E. coli*, because nFBP contains an N-terminal signal sequence that directs FBP to the periplasmic space (20). The cationic detergent CTAB was used to prepare a periplasmic extract. The method of Berish *et al.* (20) (4% CTAB extraction for 1 h at 310 K) still gave a pink pellet after centrifugation. This suggested that the extraction was not complete. After using 2% CTAB with extraction overnight, a white pellet with red supernatant was obtained after centrifugation, indicating that a complete extraction had been achieved.

The diluted cell-free extract was applied to a cation exchange column that was then eluted with a 1 M NaCl gradient. Pink fractions were eluted at 0.16 M salt and were collected. After dialysis and ultrafiltration, pink-colored high purity nFBP was obtained as shown by the SDS-PAGE gel, which had one major band at ~34 kDa (see supplemental Fig. S1 under "Supporting Information"). These profiles are similar to the FBP purified from gonococci by Mietzner *et al.* (18). Crystallization trials were successful and confirmed the high purity of the protein.

Characterization of nFBP—The molecular masses of both holo-nFBP and apo-nFBP were investigated by electrospray mass spectrometry. When the pink holo-nFBP solution was added into the mass spectrometry buffer containing 50% organic solvent (CH_3CN or CH_3OH), a red precipitate formed that dissolved after gentle shaking, giving rise to a colorless solution. However, no precipitate formed with the apo-nFBP sample. Holo-FBP had an apparent molecular mass of 33,643 Da (see supplemental Fig. S2 under "Supporting Information"),

[2] D. E. McRee, C. M. Bruns, P. A. Williams, T. A. Mietzner, and R. Nunn, unpublished data.

TABLE I
Iron and phosphorus analysis of holo-nFBP and apo-nFBP

Protein	Fe/protein molar ratio	P/protein molar ratio
Holo-nFBP	1.04 ± 0.06	0.98 ± 0.1
Apo-nFBP	not detected	0.05 ± 0.02

in agreement with the amino acid sequence (309 amino acids without iron or phosphate; theoretical mass of 33,639.39 Da). Apo-nFBP itself had an apparent molecular mass of 33,648 Da. This finding suggests that under the conditions of mass spectrometry neither holo-nFBP nor apo-nFBP had iron or synergistic anion bound to the protein and that the nFBP signal sequence had been cleaved at Asp-23 upon translocation to the periplasm.

The iron and phosphorus contents of both holo-nFBP and apo-nFBP were determined by ICP-AES. The protein concentrations (holo-nFBP, 5.83 mg/ml; apo-nFBP, 5.64 mg/ml) were measured by the BCA method using bovine serum albumin as a standard (37) and were converted into molar concentrations (holo-nFBP, 1.72×10^{-4} M; apo-nFBP, 1.67×10^{-4} M) according to their calculated molecular masses. The samples were diluted 10 times for ICP-AES analysis, and three repeat measurements were made. The iron and phosphorus contents of the proteins are listed in Table I. These data suggest that the "as purified" holo-nFBP contains 1 mol iron and 1 mol phosphorus (as the synergistic anion phosphate)/mol protein, whereas apo-nFBP contains neither iron nor phosphorus.

UV-visible Studies—UV-visible spectra of holo-FBP and apo-FBP are shown in Fig. 1. Both holo-nFBP and apo-nFBP exhibit a band with a maximum intensity at 279 nm and a shoulder near 290 nm, indicative of the presence of Trp residues. The molar extinction coefficients at 280 nm (ϵ_{280}) were determined as 44,200 $M^{-1}cm^{-1}$ for apo-nFBP and 48,900 $M^{-1}cm^{-1}$ for holo-nFBP. Apo-nFBP has no band in the visible region, whereas holo-nFBP exhibits a broad band centered near 481 nm, which gives rise to the pink color of the protein. The value of ϵ_{481} for holo-nFBP was determined to be 2,440 $M^{-1}cm^{-1}$.

NMR Spectroscopic Studies—Holo-nFBP was highly soluble in 0.1 M KCl (>7 mM), and the solution was stable at 277 K as well as at room temperature. However, apo-nFBP was much less soluble (<2 mM) and less stable at 277 K but more stable at room temperature. Precipitates formed in apo-nFBP solutions a few days after preparation, even at 0.2 mM.

^{31}P NMR investigations revealed no ^{31}P signal for either apo-nFBP or holo-nFBP. This was expected for apo-nFBP, because ICP-AES studies revealed no phosphorus associated with the apoprotein. However, ICP-AES detected one phosphorus in the holo-protein, so the absence of a ^{31}P NMR signal suggests that this phosphorus atom must be close to the paramagnetic Fe(III) center, which broadens the ^{31}P signal beyond detection. High spin $3d^6$ Fe(III) is known to be an effective NMR-broadening agent. The effects can arise from both through-space (dipolar broadening and $\propto 1/r^6$) and through-bond (contract interaction, delocalization of unpaired electrons) interactions (49).

^1H NMR spectra for both holo-nFBP and apo-nFBP are shown in supplemental Fig. S3 under "Supporting Information." Major ^1H NMR differences exist between the apo-protein and the holo-forms. For example, sharp peaks at $\delta = 7.78$ (*a*), $\delta = 7.73$ (*b*), and $\delta = 7.24$ (*c*) for apo-nFBP (as shown in supplemental Fig. S3) have disappeared from the spectrum of holo-nFBP and are probably attributed to aromatic CH protons from the residues close to Fe(III). The peaks at $\delta = -0.03$ (*d*), $\delta = -0.60$ (*e*), and $\delta = -0.65$ (*f*) in the high field region are probably from methyl groups lying below or above side chain aromatic rings (*e.g.* Trp) and are shifted by ring current effects. These peaks are broadened for holo-nFBP, suggesting that they are near to the Fe(III) or are less mobile in the holo-protein. The two-dimensional TOCSY and two-dimensional NOESY spectra of apo-FBP and holo-FBP contain many overlapping peaks because of the large size of the protein (50). More NOESY connectivities were seen for apo-nFBP than for holo-nFBP, especially in the region between 5 and 6.6 ppm (50). All of these features confirm that recombinant apo-FBP and holo-FBP are folded proteins. Further analysis of the NMR data is beyond the scope of this paper.

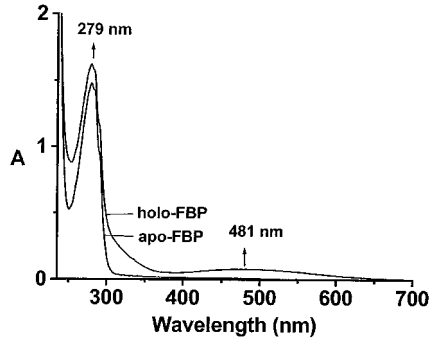

FIG. 1. **UV-visible spectra of holo-nFBP and apo-nFBP (33 μM) in 0.1 M KCl (pH 7.4).**

Anion Binding Properties of nFBP

We investigated whether nFBP from *N. gonorrhoeae* contains phosphate as a synergistic anion and whether this can be replaced by carbonate, the normal synergistic anion for transferrin, or by other anions.

UV-visible Studies—A titration of Fe(III) (as $Fe(NTA)_2$) with apo-nFBP in the presence of 5 mM phosphate (10 mM Hepes buffer (pH 7.4)) was monitored by UV-visible spectroscopy. As shown in Fig. 2*A*, a new broad band centered at 481 nm appeared immediately and increased in intensity upon the addition of Fe(III) until 1 mol eq was reached. A plot of ΔA_{481} against the molar ratio (*r*) of Fe to apo-FBP is shown in Fig. 2*B*. It can be clearly seen that with the increase in *r*, the band at 481 nm increased in intensity and reached a plateau at $r = 1$, which suggests that one mol Fe(III) binds strongly per mol nFBP.

Similar experiments were performed using other anions (pyrophosphate, (bi)carbonate, oxalate, and NTA) instead of phosphate. In all of these cases, Fe(III) bound strongly to nFBP with a 1:1 molar ratio. A distinctive position of the LMCT (Tyr→Fe(III)) band was observed as shown in Fig. 3 and Table II. The wavelength of the LMCT band of transferrin is known to be sensitive to the nature of the anion including the substitution of carbonate by glyoxylate or glycine (51, 52). This finding suggests that both carboxylates and phosphates can act as synergistic anions for nFBP. The wavelength of the LMCT band in the presence of phosphate is the same as the band for the native protein (481 nm), suggesting that phosphate is the native synergistic anion. A titration performed in physiological buffer (100 mM NaCl, 4 mM phosphate, and 25 mM bicarbonate (pH 7.4)) gave rise to a LMCT band at 481 nm, which suggests that phosphate is the bound anion under these conditions. Phosphate binding was also confirmed by the anion exchange studies described below.

A titration of $Fe(NTA)_2$ as the Fe(III) source with apo-nFBP in 0.1 M KCl but in the absence of any added synergistic anion gave rise to a specific band at 457 nm. This implies that NTA can also act as a synergistic anion. NTA is known to be able to act as a synergistic anion in transferrins (51, 52), confirmed by

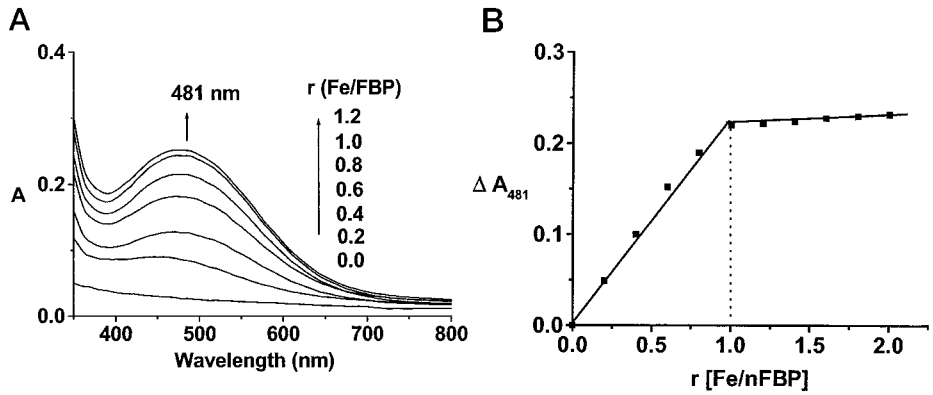

FIG. 2. **Titration of apo-nFBP with Fe(III).** *A*, UV-visible spectra of apo-nFBP (84 μM) and after addition of [$Fe(NTA)_2$] (0, 0.2, 0.4, 0.6, 0.8, 1.0, 2.0 mol eq) in 10 mM Hepes, 5 mM NaH_2PO_4 (pH 7.3), 298 K. *B*, titration curve for binding of Fe(III) to apo-nFBP based on the intensity of the LMCT band of Fe-PO_4-nFBP at 481 nm (conditions as above).

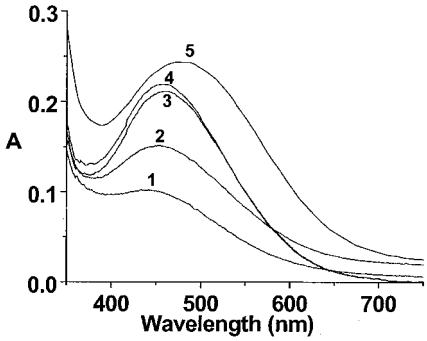

FIG. 3. **UV-visible spectra of Fe·nFBP in the presence of different synergistic anions.** Conditions: 1.0 mol eq of [$Fe(NTA)_2$] was added to 33–84 μM apo-nFBP in 10 mM Hepes buffer (pH 7.3), 5 mM anion, 298 K. Anions are pyrophosphate (*1*), oxalate (*2*), carbonate (*3*), NTA (*4*), and phosphate (*5*).

TABLE II
Characteristics of the ligand-to-metal charge transfer band of Fe-nFBP in the presence of various synergistic anions[a]

	Anion[a]				
	Phosphate	Pyrophosphate	Carbonate	Oxalate	NTA
λ_{max} (nm)	481	439	459	451	457
ε (M^{-1} cm^{-1})	2440	1650	2750	3050	2780

[a] Conditions: 1–2 mol eq $Fe(NTA)_2$ was added to apo-nFBP (33–84 μM) in the presence of 5 mM anion, 10 mM Hepes, pH 7.3, at 298 K.

the recent 2.1 Å resolution x-ray crystal structure of an Fe(III)-ovotransferrin-NTA ternary complex (53). The wavelength of the LMCT band of Fe(III)-NTA-hTF (465 nm) is the same as that for Fe(III)·CO_3-hTF (52). Therefore, it is reasonable that λ_{max} for the LMCT band of Fe(III)-NTA-nFBP is similar to that for Fe(III)·CO_3·nFBP (~459 nm).

Because Fe(III) can be loaded into hTF by the addition of Fe(II) to air-saturated solutions of the apo-protein (54), we titrated apo-nFBP with Fe(II) ammonium sulfate in the absence of other added anions. The oxidation of Fe(II) to Fe(III) appeared to be accelerated by the presence of nFBP and led to a weak Fe·nFBP complex with a λ_{max} of 472 nm. The saturation of nFBP was complete after the addition of ~3 mol eq of Fe(II) (as judged by the ratio A_{470}/A_{400}). Because this is not the wavelength of the Fe·CO_3·nFBP complex, we conclude that ambient bicarbonate (~0.14 mM (pH 7.4), 298 K (55)) is not able to promote the formation of an Fe(III)·CO_3·nFBP complex. The identity of the bound anion(s) in Fe·nFBP formed via Fe(II) oxidation is unknown but could be hydroxide, and it is possible that such a complex is unstable via the loss of iron as ferric hydroxide. The experiments described below appear to rule out sulfate as a bound anion.

Titrations of $Fe(NTA)_2$ with apo-nFBP were performed in the presence of sulfate or perchlorate to see whether they can serve as synergistic anions. LMCT bands centered at ~458 nm were observed but were ascribed to bound NTA (ϵ_{458} ~2,800 $M^{-1}cm^{-1}$) as the synergistic anion. Moreover, phosphate exchange studies on Fe-PO_4-nFBP monitored by ^{31}P NMR (described below) also do not support sulfate or perchlorate as a synergistic anion for Fe·nFBP.

Synergistic Anion Exchange

UV-visible Studies—Fe·CO_3·nFBP was prepared by mixing 1.0 mol eq of $Fe(NTA)_2$ with apo-nFBP (83 μM) in the presence of a large excess of HCO_3^- (5 mM). The broad band at ~459 nm was indicative of the formation of the Fe·CO_3·FBP. Upon the addition of phosphate (final concentration of 5 mM) to this solution, the LMCT band shifted to 481 nm over a period of 30 min (see Fig. 4). This finding suggested that bound carbonate is readily displaced by phosphate. Similar experiments were also performed with Fe-oxalate-nFBP (oxalate as synergistic anion). When phosphate (final concentration of 5 mM) was added to the Fe-oxalate-nFBP, the LMCT band decreased in intensity and shifted from 451 to 481 nm over a period of 30 min, suggesting that the synergistic anion oxalate was displaced by phosphate.

UV-visible studies were also performed to see whether phosphate in native nFBP can be displaced by carbonate. As shown in Fig. 5*A*, when a 200-fold molar excess of $NaHCO_3$ was added to native nFBP solution (0.11 mM, 0.1 M KCl (pH 8.0)), the LMCT band of native FBP gradually shifted from 481 to 460 nm and increased in intensity over a period of 5 h. This finding suggests that phosphate in nFBP has been displaced and that Fe·CO_3·nFBP has formed.

Similar experiments were also performed using a 400-fold molar excess of sulfate or perchlorate instead of bicarbonate; however, no shifts of the LMCT band of the native nFBP were observed.

^{31}P NMR Studies—To confirm that the synergistic anion (hydrogen) phosphate can be displaced by (bi)carbonate, ^{31}P NMR studies were carried out. When a 50-fold molar excess of $NaHCO_3$ (pH 8.0) was added to a solution of native holo-nFBP (1 mM (pH 8.0), 0.1 M KCl), no ^{31}P NMR peak appeared after incubation for 12 h at 298 K, which suggests that phosphate binds strongly to Fe·nFBP. However, when a 200-fold molar excess of $NaHCO_3$ was added, a new ^{31}P NMR peak appeared at 3.23 ppm and grew to its maximum intensity 24 h later (see Fig. 5*B*). This peak has a chemical shift characteristic of free phosphate (56, 57). This confirms that phosphate is the native synergistic anion in nFBP and that it can be displaced by a large excess of carbonate. To confirm that phosphate was displaced, the sample was ultrafiltered. A colorless filtrate was obtained, which gave a ^{31}P NMR peak at 3.23 ppm (*i.e.* free phosphate).

In contrast, after the addition of a 400-fold molar excess of Na_2SO_4 or $NaClO_4$ to solutions of holo-nFBP and incubation for

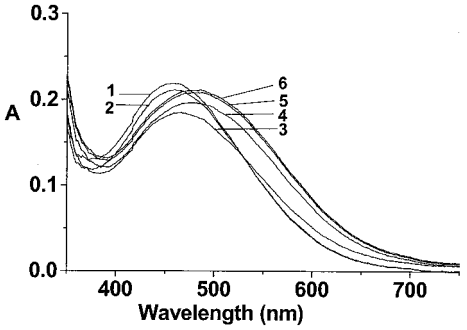

FIG. 4. **Displacement of carbonate from Fe·CO_3·nFBP by phosphate.** UV-visible spectra showing the shift of the LMCT band at various times after adding 5 mM NaH_2PO_4 to 83 μM Fe·CO_3·FBP in 10 mM Hepes, 50 mM KCl, 5 mM $NaHCO_3$ (pH 7.3) at 298 K. *1*, Fe·CO_3·FBP; *2*, 1 min; *3*, 10 min; *4*, 20 min; *5*, 30 min; and *6*, 1 h after the addition of 5 mM NaH_2PO_4. The shift of the LMCT band from 460 to 481 nm is indicative of displacement of the synergistic anion carbonate by phosphate.

3d at 298 K, no ^{31}P NMR peak appeared. This together with the UV studies suggests that neither sulfate nor perchlorate can act as a synergistic anion for Fe·nFBP.

EXAFS Comparison of Phosphate-Fe·nFBP and Carbonate-Fe·nFBP

FeK-edge EXAFS studies were carried out to investigate the local structural differences between Fe·PO_4·nFBP and Fe·CO_3·nFBP. The edge structure (XANES) and edge positions were the same for Fe·PO_4·nFBP and Fe·CO_3·nFBP, and their positions are consistent with the expected 3+ oxidation state for Fe. However, the spectra differ markedly in other respects (see Fig. 6). The amplitude of the EXAFS oscillations for Fe·PO_4·nFBP dies away with increasing k, whereas the amplitude for the Fe·CO_3·nFBP EXAFS is relatively even throughout its range. This results in significant differences in the corresponding Fourier transforms, which are not the result of the different EXAFS data ranges available for the calculation of the Fourier transforms (see supplemental Fig. S4 under "Supporting Information"). The Fourier transform for Fe·PO_4·nFBP shows two overlapping peaks of similar intensity, whereas that for Fe·CO_3·nFBP is dominated by a single peak with a shoulder on the longer distance side. The two overlapping peaks for Fe·PO_4·nFBP can be simulated with two oxygen backscatterers at an average distance of 1.94 Å and four oxygen/nitrogen backscatterers at an average distance of 2.12 Å. The fit is slightly improved if the nitrogen is allowed to refine to a separate (2.24 Å) distance. The EXAFS for Fe·CO_3·nFBP refines to four donor ligands at an average distance of 1.98 Å and two ligands at 2.20 Å (the shoulder in the Fourier transform). These peaks are the result of scattering from the atoms directly coordinated to Fe(III). The first shell peak in the Fourier transform is considerably more intense for the carbonate adduct than the phosphate adduct. This is reflected in the corresponding Debye-Waller factors ($2\sigma^2 = 0.001$ and 0.004, respectively). This is not an artifact of data collection. Both data sets were collected at the same temperature, and the total count rate on the fluorescence detector was kept approximately the same for both samples (half of the maximum linear count rate). This finding suggests that the ligands are significantly more ordered with respect to the metal with CO_3 bound compared with PO_4.

Despite the difference between the spectra, both data sets have a peak in their respective Fourier transforms at ~2.6 Å for which the crystal structures have no obvious candidate atoms. The Fe·PO_4·nFBP data also have a peak at 3.2 Å, which is at the correct distance for the phosphorus of the synergistic phosphate ligand. Although these data together with the significant difference in the first shell appear to confirm that the two nFBP samples have different synergistic anions, it must be remembered that in addition to small "rigid" ligands such as phosphate and carbonate, the atoms of the Tyr and His ligands contribute significant multiple scattering in the 3–6 Å range. Because the ligand bond lengths are different between the two samples, the Tyr and His multiple scattering patterns will also differ. Thus, it is the different distribution of ligand bond lengths and pattern of peaks in the 3–6 Å range that supports the notion of different synergistic anions. To confirm this finding, the constrained and restrained full multiple scattering analyses in three-dimensional space were carried out using all the well ordered atoms of the ligand residues within 5 Å of the central atom.

Multiple Scattering EXAFS Analysis

EXAFS simulations of the Fe·PO_4·FBP data using the hFBP and nFBP crystallographic coordinates gave very poor results (R-factors of 60.9% and 73.4%, respectively) (see supplemental Fig. S5). Given the difference in the estimated errors between the two techniques (~0.1–0.2 Å for the crystal structures; ~0.02 Å for EXAFS), this is not particularly surprising. A comparison of the two sets of crystallographic coordinates (see Table IV) reveals significant disagreement in the Fe-ligand bond lengths. The nFBP structure gives both Fe-Tyr bond lengths as similar (1.84 and 1.88 Å), whereas the hFBP structure suggests a large split (0.14 Å) with one very short Fe-tyrosine bond (1.78 Å). The two structures also differ by 0.21 Å in the Fe-OH_2 bond length. The Fe·PO_4·nFBP EXAFS data do not support the short Fe-Tyr distance of the hFBP crystal structure. With the hFBP coordinates, the R-factor can be reduced from 61 to 42% by changing the Fe-Tyr-195 bond length from 1.78 to 1.9 Å, which is similar to the Fe-Tyr-196 distance and more typical of iron-tyrosinate systems. On (constrained) refinement of the Fe-ligand bond lengths (using either coordinates), the Fe-OH_2 distance refines to 2.10 Å, slightly longer than the 2.02 Å of the hFBP crystal structure but still significantly shorter (by 0.13 Å) than the distance suggested by the nFBP crystal structure. For the constrained refinement, a total of 13 parameters were initially varied: the Fermi energy, 6 Fe-ligand bond lengths, 5 Fe-ligand angles, and the Debye-Waller factor for ligand-bonded (first shell) atoms. At this stage, the best fit obtainable had an R-factor of 30.5% and did not adequately simulate the peak at 2.6 Å in the Fourier transform or the EXAFS data between 7 and 9 $Å^{-1}$. Because the 2.6 Å peak is also present in the Fe·CO_3·nFBP data, it was concluded that it was not likely to be attributable to the synergistic phosphate anion. There is no independent evidence to suggest an additional unidentified ligand at this distance. To check whether the assignment of the ligands to the six refined distances were correct, the ligands were systematically swapped to the other five distances, and the refinement was repeated. This finding revealed a number of false minima with R-factors of 33–35%, but none improved upon the fit to the 2.6 Å peak. Therefore, it was necessary to consider what more significant changes from the crystal structure might be responsible for this difference. The simulation of the "outer" multiple scattering peaks (3–5 Å) was good. 3–5 Å peaks result largely from the multiple scattering from the Tyr and His rings. Therefore, attempts to model the 2.6 Å peak by decreasing the Fe-ligand angles for the Tyr and His rings all resulted in significantly worse fits. Attempts were made to model a "bidentate" phosphate by (*a*) removing the water and rotating the phosphate group to place the oxygen closest to the water at this position and (*b*) rotating the phosphate group to place an oxygen in the 2.6 Å Fourier transform peak. In both cases, this resulted in high R-factors and very poor fits to the EXAFS,

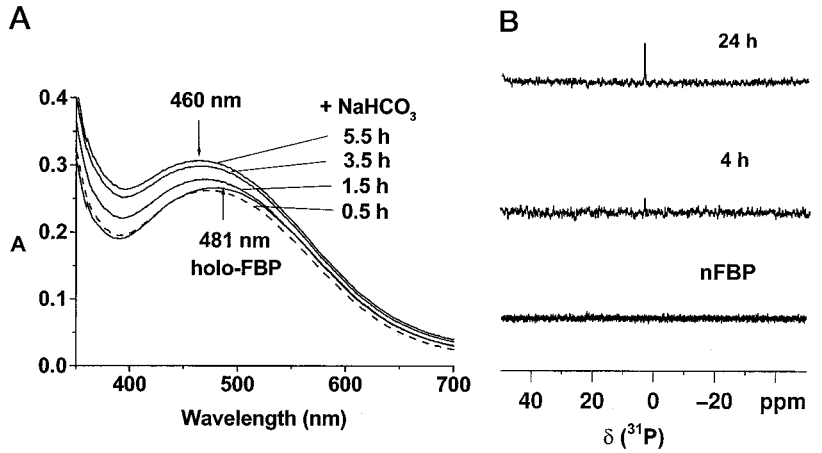

FIG. 5. **Displacement of phosphate from Fe·PO_4·nFBP by carbonate.** *A*, UV-visible spectra of Fe·PO_4·nFBP (0.11 mM) and 0.5, 2.5, 3.5, and 5.5 h after the addition of 20 mM $NaHCO_3$ at 298 K in 0.1 M KCl (pH 8.0). The shift of the LMCT band from 481 to 460 nm is indicative of the slow substitution of the synergistic anion phosphate by carbonate. *B*, ^{31}P NMR spectrum of holo-nFBP (1 mM in 0.1 M KCl (pH 8.0), 298 K) before and after the addition of a 200-fold molar excess of $NaHCO_3$ at various times. The appearance of the peak at 3.23 ppm (characteristic of free phosphate) after the addition of $NaHCO_3$ is indicative of displacement of the synergistic anion phosphate by carbonate. For holo-nFBP, the ^{31}P resonance is broadened beyond detection by the paramagnetic effects of Fe(III).

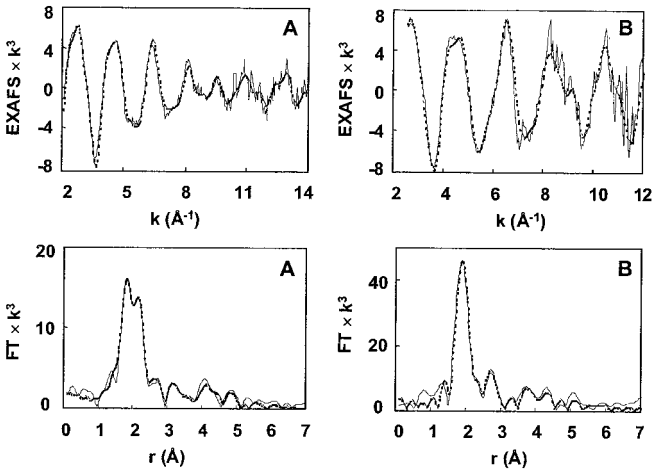

FIG. 6. **Comparison of the final restrained EXAFS fit for Fe-FBP with phosphate and carbonate as bound anions.** EXAFS spectra (*top*) and Fourier transforms (*bottom*) of Fe·PO_4·nFBP (*A*) and Fe·CO_3·nFBP (*B*) are shown. *Solid line*, experimental; *dotted line*, calculated. The *k* ranges used for the calculating the Fourier transforms were 13.1 and 11.1 Å $^{-1}$ for Fe·PO_4·nFBP and Fe·CO_3·nFBP, respectively. A comparison of the Fourier transforms calculated using the same *k* range can be seen in supplemental Fig. S4 under "Supporting Information."

partly because of the easily identified P-atom being at the wrong distance. Clearly, as a "single atom" ligand, the $-OH_2$ cannot make any contribution to the 2.6 Å peak. This left Glu-57 as the only possible ligand that could account for the scattering at 2.6 Å. Additionally, unlike the other ligands, the side chain of glutamate has significant rotational freedom. The EXAFS-refined and starting models were examined using the molecular modeling program XFIT (part of the XtalView package) (58). This examination suggested that a rotation of the terminal portion of the side chain of Glu-57 could place atoms at the correct distances to account for the unfilled 2.6 Å peak in the Fourier transform. This rotation could be achieved in two ways. (i) The same rotamer is maintained, but the terminal position is rotated around the CG–CD bond (this maintains the residue at approximately the same position with respect to the other ligands). (ii) Select the rotamer (using the XFIT in-built rotamer library) that most closely gives the desired bond distances to the iron. For method (i), a series of multidimensional maps of the position of these atoms (still treating the ligand as a rigid body) against EXAFS Fit Index were calculated. They strongly supported the notion that such a rotation together with a small translation (to maintain the correct first shell bond length for Glu) would lead to a satisfactory fit to the EXAFS data. This change in the position of Glu-57 immediately led to a significant reduction in the *R*-factor from 30 to under 26% and good fits to both the EXAFS and Fourier transforms. A further reduction in the *R*-factor (to 23.9%) was then obtained by refining the position of Glu-57 together with the original parameters for the other five ligands, giving the constrained fit in Table III. The deviation of the CG-CD vector in this model from its initial position arose during the final constrained refinement of all 14 parameters as the Fe-OE1-Glu angle was refined.

The model derived above was obtained by a left-handed rotation around the CG-CD vector as orientated in Fig. 7. This places the Fe-bonded oxygen (OE1) closer to the phosphate ligand and the longer oxygen (OE2) closer to His-9. Equally valid is the opposite rotation placing Fe-bonded OE1 closer to His-9 and the longer OE2 closer to the phosphate. On constrained refinement, such a model gives an acceptable *R*-factor of 24.8%. Constrained refinement using the alternative rotamer model (as described in (ii) above) also gave an acceptable fit but with a slightly higher *R*-factor (25.2%). Because it gave the best fit, only the model derived by a left-hand rotation of Glu-57 around the CG-CD vector was analyzed further.

Restrained refinement against ideal bond lengths (47) led to a further reduction in the *R*-factor (from 23.9 to 20.5%) without any significant changes to the model (see Tables III and IV and Fig. 7). The restrained refinement was well determined with a parameter/observation ratio of 2.0.

It was necessary to keep the six ligand distances separate until the final stages of the refinement to accommodate the changes in Fe-ligand distances from the initial model. This also allowed for the comparison with the crystallographic distances. An examination of the EXAFS-derived distances for the Fe-PO_4-FBP data shows these distances as falling into three distinct groups: 1) Tyr-195 and Glu-57 (1.93 and 1.95 Å, distance correlation 0.8), 2) Tyr-196, water, and phosphate (2.08, 2.10, and 2.13 Å, distance correlation 0.7–0.8), and 3) His-9 (2.28 Å). The distance correlations among these three groups were low (0.05–0.2). Therefore, the effects on both the constrained and restrained models of allowing only three Fe-ligand distances were examined. This resulted in marginally higher final fit indices and *R*-factors with distances as expected at average values with respect to the six-distance refinement (see Tables III and IV). In the restrained refinement, some of the effect of this averaging is accommodated by a small increase in the deviation from ideal geometry. Relaxing the bond length restraints resulted in unrealistic and unacceptable deviations from the known internal geometry of the ligands. Also, it did not lead to the simulation of the 2.6 Å peak.

The nFBP crystal coordinates suggest a similar distance for the two tyrosine ligands, whereas the EXAFS data for Fe-PO_4-FBP suggest a large split (0.15–0.17 Å). This split is similar to

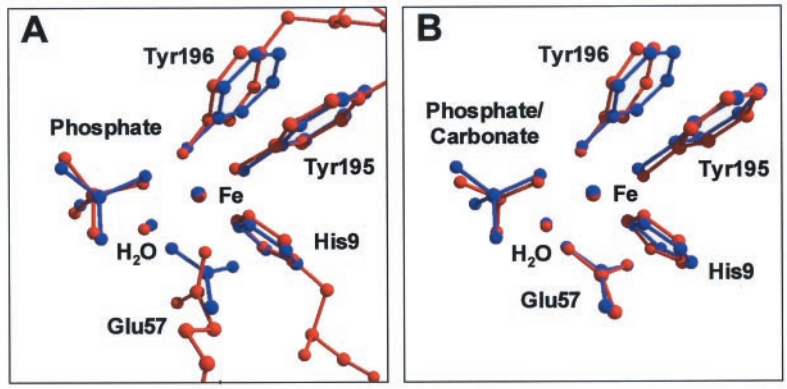

FIG. 7. **The Fe binding site in Fe-FBP.** A comparison of the EXAFS model for Fe·PO_4·nFBP (*blue*) with the crystal structure of Fe- PO_4-hFBP (*red*) (*A*) and the EXAFS model for Fe·PO_4·nFBP (*blue*) with the EXAFS model for Fe·CO_3·nFBP (*red*) (*B*) is shown.

TABLE III
Statistics for different EXAFS models for Fe·PO_4·nFBP and Fe·CO_3·nFBP

	Fe·PO_4·nFBP		Fe·CO_3·nFBP	
k Range (Å^{-1})	13.1		11.1	
Crystal structure fit	hFBP	nFBP		
Ni/*p*[a]	33	33		
Fit index[b]	17.3	27.2		
R-factor (%)[c]	60.9	73.4		
Constrained fit				
Before rotation of Glu^{57}	6 distances	3 distances[d]	6 distances	3 distances[e]
Ni/*p*[a]	2.5	—	—	—
Fit index[b]	5.14	—	—	—
R-factor (%)[c]	30.5	—	—	—
After rotation of Glu^{57}				
Ni/*p*[a]	2.4	2.4	1.9	1.9
Fit index[b]	3.56	4.03	6.02	6.12
R-factor (%)[c]	23.9	25.7	26.6	26.9
Restrained fit				
Ni/*p*[a]	2.0	2.0	2.0	2.0
Fit index[b]	0.59	0.61	1.35	1.42
R-factor (%)[c]	20.5	20.9	24.4	25.5
Deviation from Engh and Huber distances (%)	1.05	1.18	0.92	1.00
υ[f]	45	45	41	41
$(\Delta\chi)^2$ $[(\Delta\chi)^2_\upsilon]$[g]	52 [1.16]	55 [1.22]	48 [1.17]	51 [1.24]

[a] *Ni* is the number of independent data points; *p* is the number of refined parameters (including those that were refined at previous stages of the analysis).
[b] Fit index $\phi = \Sigma_i(1/\sigma_i^2)\{k^3[\chi^{exp}(k_i) - \chi^{th}(k_i)]\}^2$ where $\sigma = \Sigma_j k^3|\chi^{exp}(k_j)|$ and χ^{exp} and χ^{th} are the experimental and theoretical EXAFS, respectively.
[c] *R*-factor $= \Sigma_i^N(1/\sigma_i)k^3|\chi^{exp}(k_i) - \chi^{th}(k_i)| \times 100\%$.
[d] Because of correlation, ligands were grouped into three distances: Glu^{57}/Tyr^{195}, Tyr^{196}/PO_4/H_2O, and His^9.
[e] Because of correlation, ligands were grouped into three distances: Tyr^{195}/Tyr^{196}, Glu^{57}/H_2O, and His^9/CO_3.
[f] υ is the number of degrees of freedom, $\upsilon = Ni - p$.
[g] $(\Delta\chi)^2$ is as defined in Ref. 48 and should be $\cong \upsilon$. $(\Delta\chi)^2_\upsilon$ should $\rightarrow 1$.

that in the hFBP coordinates, but both tyrosines are displaced to longer distance by ~0.15 Å. Attempts to model the similar Fe-tyrosine distances of the nFBP coordinates in the Fe-PO_4-FBP EXAFS data (using both the original and EXAFS-derived rotation of Glu-57 with Tyr-196 and Glu-57 distances swapped) resulted in very poor fits and high *R*-factors, even after extensive refinement.

Fe-EHPG has been widely used as a model for transferrins (59, 60), because it contains 2 amino, 2 phenoxy, and 2 carboxyl groups in a single hexadentate binding site. It is also a useful model for FBPs. EXAFS data for Fe-EHPG were used to test the validity of the method used to fit the Glu residue in the FBP EXAFS data. Starting with the crystal structure (45), the phenyl rings and carboxyl groups were individually tilted away from their initial (correct) positions by up to 60°. The rest of the structure then was refined against the EXAFS data using multiple scattering and restrained refinement,[3] and finally, the maps of the "tilt angle" against other refined parameters were calculated. The back atoms of the phenyl rings were too far from the central atom (4.7–5.6 Å) for small angular tilts (<30°) to have any significant effect on the fit. However, the carboxyl group with its carbon at 2.85 Å is a better analogy to the Glu residue in the FBP structure. This proved much more sensitive to angle in all cases, finding the original angular position of the carboxyl group to within 5–10°. This finding supports the case that with this type of multiple ring-containing site, the use of multiple scattering with constraints/restraints does allow the orientation of a carboxyl (or similar) ligand to be determined with confidence.

For the Fe·CO_3·nFBP EXAFS data, the PO_4 of the model was replaced with an idealized CO_3, placing the bonding oxygens of the two ligands at the same positions and the carbon of CO_3 along the phosphate (Fe)O–P axis. The carbonate was rotated around the (Fe)O–C axis, and a clear minimum was found. By analogy with the Fe-PO_4-FBP EXAFS, attempts to model a bidentate CO_3 resulted in high *R*-factors and poor fits to the EXAFS. The situation and solution with Glu-57 were identical to the Fe-PO_4-nFBP case. Also analogous with the Fe-PO_4-FBP data were the correlations for the six separate Fe-ligand distances. The groups found were Tyr-195/Tyr-196 (both 1.96 Å),

[3] Distance-based constrained refinement with distance refinement is not appropriate for the EHPG ligand as the constraints will also prevent any metal-ligand distance changes.

TABLE IV
A comparison of the bond lengths (r(Å)) and angles (°) for Fe-FBP determined from EXAFS data using "ideal" restraints for Fe-PO_4-nFBP and Fe-CO_3-nFBP and by x-ray crystallography

Ligand	Crystal structures				EXAFS							
	Fe-PO_4-hFBP (PDB code 1MRP)		Fe-CO_3-nFBP (PDB code 1D9Y)		Fe-PO_4-nFBP				Fe-CO_3-nFBP			
					6-ligand distances		3-ligand distances[a]		6-ligand distances		3-ligand distances[b]	
	r(Å)	*angle (°)*	*r(Å)*	*angle (°)*	*r(Å)*	*angle (°)*	*r(Å)*	*angle (°)*	*r(Å)*	*angle (°)*	*r(Å)*	*angle (°)*
His^9 (N)	2.19	117	2.19	118	2.28 ± 0.01	115 ± 2	2.28 ± 0.02	114 ± 2	2.21 ± 0.04	112 ± 4	2.22 ± 0.01	113 ± 3
Glu^{57} (O)	2.08	131	2.03	134	1.95 ± 0.01	98 ± 1	1.94 ± 0.01	98 ± 1	2.00 ± 0.03	97 ± 1	2.03 ± 0.02	97 ± 1
Tyr^{195} (O)	1.78	150	1.84	141	1.93 ± 0.01	142 ± 1	1.94 ± 0.01	141 ± 1	1.96 ± 0.03	147 ± 5	1.96 ± 0.01	147 ± 3
Tyr^{196} (O)	1.92	124	1.88	121	2.08 ± 0.04	114 ± 1	2.11 ± 0.01	112 ± 1	1.96 ± 0.04	125 ± 4	1.96 ± 0.01	124 ± 2
PO_4/CO_3 (O)	2.09	133	2.10	144	2.13 ± 0.01	133 ± 1	2.11 ± 0.01	133 ± 1	2.19 ± 0.04	119 ± 2	2.22 ± 0.01	115 ± 2
H_2O (O)	2.02	N/A	2.23	N/A	2.10 ± 0.04	N/A	2.11 ± 0.01	N/A	2.06 ± 0.02	N/A	2.03 ± 0.02	N/A

[a] Because of correlation, ligands were grouped into three distances: Glu^{57}/Tyr^{195}, $Tyr^{196}/PO_4/H_2O$, and His^9.
[b] Because of correlation, ligands were grouped into three distances: Tyr^{195}/Tyr^{196}, Glu^{57}/H_2O, and His^9/CO_3.

Glu-57/H_2O (2.00 Å, 2.06 Å, respectively) and CO_3/His-9 (2.19 Å, 2.21 Å, respectively). The correlations in the six-distance refinements suggest that it is safer to model both EXAFS data sets using only three Fe-ligand distances (see Tables III and IV).

An absolute index of the goodness of fit, which takes into account the degree of overdeterminancy of the EXAFS fit, is given by the reduced χ^2 function $(\Delta\chi)^2_\upsilon$. For an acceptable fit, $(\Delta\chi)^2$ should be approximately equal to υ, the number of degrees of freedom, and therefore, $(\Delta\chi)^2_\upsilon$ should tend to 1. Values for υ, $(\Delta\chi)^2$ and $(\Delta\chi)^2_\upsilon$ for the final fits are given in Table III. As the values of $(\triangle\chi)^2$ are approximately equal to υ, the fits are acceptable on a statistical basis, and statistical rather than systematic errors dominate (as may be expected for this type of data). This finding suggests that the uncertainties given in Table IV adequately represent the uncertainties of the best-fit parameter values. These uncertainties were calculated by varying a parameter away from its optimal value while optimizing all other parameters until $(\triangle\chi)^2$ increased by 1 above its minimum value (48). Uncertainties calculated by this method were compared with values obtained using a co-variance matrix. These two methods should be equivalent and after rounding gave the same estimates for the uncertainties.

Examination of the resulting models for both phosphate and carbonate anions (Fig. 7) suggests a possible reason why nFBP has the synergistic anion bound in a monodendate mode. In its suggested new position, OE1 of Glu-57 is well placed to form a strong hydrogen bond (2.1 Å, O–H–O angle 113°) to the Fe-bound water at 2.07–2.1 Å. Additionally, Glu-57 may form hydrogen bonds to PO_4 and CO_3 synergistic anions if they are protonated. This potential hydrogen-bonding network remains intact with both of the other methods discussed for positioning Glu-57. The hydrogen bond lengths and angles vary but are within the normal range. Thus, there appears to be a structural reason why nFBP, unlike transferrin, binds anions in a monodentate mode. The glutamate side chain carboxylate group of nFBP is part of a hydrogen-bonding network, which both locks in the Fe-bound water and stabilizes the synergistic anion in a monodentate configuration.

Metal Binding to nFBP—Transferrin can bind strongly to metal ions such as Ga(III), Co(III), and Bi(III) in its specific iron sites (63). Therefore, investigations were made to determine whether these metal ions can also bind to nFBP. Metal ion binding to the phenolate groups of the two tyrosine residues in the specific iron sites of apo-TF leads to two new absorption bands near 241 and 295 nm because of the perturbations of the π-π^* transitions of the aromatic rings (61). This effect has been used to monitor specific metal binding to transferrins by UV-visible difference spectroscopy (13), and therefore was used here to investigate the binding of Ga(III), Bi(III), and Co(III) to apo-nFBP.

Ga(III) Binding—The addition of $Ga(NTA)_2$ to apo-nFBP in 10 mM Hepes (pH 7.3) solution containing 5 mM phosphate at 298 K resulted in two new absorption bands near 245 and 298 nm in the UV difference spectrum. The spectra are characteristic of metal-tyrosyl coordination and are similar to those reported for Ga-transferrin complexes (55, 61), suggesting that Ga(III) binds to the specific iron site in apo-nFBP. A series of typical UV difference spectra is shown in supplemental Fig. S6*A* under "Supporting Information." A plot of ΔA_{245} as a function of r, the molar ratio of total Ga(III) to total FBP, is shown in supplemental Fig. S6*B* under "Supporting Information." The non-linear increase in ΔA_{245} for points below $r = 1$ and the continued increase in ΔA_{245} for points beyond $r = 1$ imply that the binding of Ga(III) to apo-nFBP is rather weak,

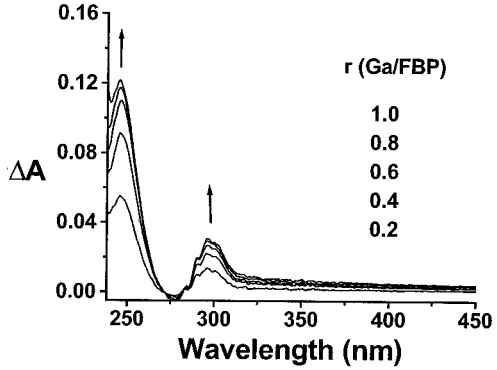

FIG. 8. **UV difference spectra for Ga(III) binding to apo-FBP.** $Ga(NO_3)_3$ (0.2, 0.4, 0.6, 0.8, and 1.0 mol eq) was added to 16.6 μM apo-FBP in 10 mM Hepes, 5 mM NaH_2PO_4 (pH 7.3), 298 K. The larger increase in the intensity of the two absorption bands at 245 and 298 nm compared with $Ga(NTA)_2$ (see supplemental Fig. S5) indicates that NTA is a strong competitor for Ga(III) binding.

so that excess Ga(III) is needed to saturate the site of apo-nFBP.

The weak binding of $Ga(NTA)_2$ to apo-nFBP may be attributed to NTA competition (Ga(NTA), log K_{ML} = 16.20). To test this possibility, apo-nFBP was titrated with $Ga(NO_3)_3$ (1.43 mM, prepared by dilution and adding NaOH to gallium atomic absorption standard solution to give pH 2.16) under similar conditions in the absence of any chelating ligands. Ga(III) binding to the specific iron site in apo-nFBP was observed as evidenced by the appearance of two new absorption bands near 245 and 295 nm in the UV difference spectrum (see Fig. 8). The binding was now stronger as evidenced by the more intense bands at 245 and 298 nm ($\Delta\epsilon_{245}$ = 8,610 $M^{-1}cm^{-1}$ by r = 2). This shows that NTA does compete with apo-FBP for Ga(III) binding. However, the increase in ΔA_{245} for points below, r = 1 is still non-linear and still continued to increase beyond r = 1. This implies that binding of Ga(III) to apo-nFBP is not strong. The $\Delta\epsilon$ values are much lower than those for Ga_2-transferrin ($\Delta\epsilon_{242}$ ~34,000 $M^{-1}cm^{-1}$) and Ga_2-lactoferrin ($\Delta\epsilon_{242}$ ~30,000 $M^{-1}cm^{-1}$) in the absence of chelating agent (55, 62), implying that the Ga-nFBP binding is weaker than Ga-transferrin or Ga-lactoferrin binding. Such weak binding in the absence of any competing ligand is probably related to the hydrolytic properties of the Ga(III) ion. In aqueous solution near pH 7.4, the major unchelated gallium species is $Ga(OH)_4^-$ and the weak binding of Ga(III) to apo-FBP may be attributed to the competition between apo-FBP and OH^- ($Ga(OH)_4^-$, $\beta_4OH = 10^{-16.6}$ (62)) as discussed previously for Ga-transferrin interactions (55).

Co(III) Binding—Apo-FBP was titrated with $[Co(III)(CO_3)_3]^{3-}$ in 10 mM Hepes buffer (pH 7.4) in the presence of 5 mM carbonate or 5 mM phosphate. However, no new bands appeared in the UV difference spectra. This suggested that specific binding of Co(III) to apo-nFBP is very weak under these conditions or too slow to be observed.

Bi(III) Binding—Titrations of Bi(NTA) with apo-FBP were performed in 10 mM Hepes (pH 7.3) in the presence of 5 mM phosphate (see supplemental Fig. S7 under "Supporting Information") or bicarbonate at 298 K. Specific binding was observed as evidenced by the appearance of two new absorption bands near 244 and 297 nm in the UV difference spectrum. However, as for Ga(III), the much smaller increase in intensity of the bands at 297 and 244 nm ($\Delta\epsilon_{244}$ ~4,060 $M^{-1}cm^{-1}$ by r = 1) compared with Bi-hTF(N-lobe) ($\Delta\epsilon_{241}$ ~22,000 $M^{-1}cm^{-1}$ (63)) or Bi_2-hTF ($\Delta\epsilon_{241}$ ~21,900 $M^{-1}cm^{-1}$/Bi (63)) suggests that binding is rather weak.

DISCUSSION

The successful overexpression of nFBP in *E. coli* and the subsequent highly efficient purification from a periplasmic extract by cation exchange column chromatography gave a high yield of recombinant nFBP (~100–200 mg from 1 liter of cell culture). Electrospray mass spectra showed essentially the same molecular mass for both holo-nFBP and apo-nFBP (33,643 and 33,648 Da, respectively), which agrees with the predicted molecular mass of 33,639 kDa. This confirms that the nFBP N-terminal signal sequence was recognized, efficiently processed, and cleaved to give a mature protein of 309 amino acids. Also the data show that no metal or synergistic anion was bound to the protein under mass spectrometric conditions, *i.e.* low pH (<4) in the presence of 50% CH_3OH. The release of metal was also supported by the formation of a pink holo-FBP precipitate upon the addition of 50% CH_3OH, which subsequently redissolved with the formation of a colorless solution. Holo-nFBP is more soluble than apo-nFBP in aqueous solution, but the opposite is true for solutions containing organic solvents, which suggest that apo-nFBP is more hydrophobic than holo-nFBP. A comparison of the recently determined crystal structure of apo-hFBP (64) with that of holo-FBP (9) reveals that large conformational changes occur upon the removal of the metal ion from the protein. Similar changes are likely to occur for nFBP.

The crystal structure of hFBP (9) suggests that Fe coordinates to phosphate. However, the protein purification process involved washing FBP-containing cells in phosphate-buffered saline, a process that could result in synergistic anion exchange in FBP (2). Also, it is difficult to distinguish phosphate from its isostructural analogue sulfate by x-ray crystallography. In a recent ^{31}P NMR study of FBP (17), FBP-containing cells were again washed with phosphate, and holo-FBP was reconstituted from apo-FBP in the presence of 50 mM phosphate. Also, it was surprising that phosphate bound to paramagnetic Fe(III) gave rise to a resolvable ^{31}P NMR peak. In transferrin, the ^{13}C resonances of bound (^{13}C) carbonate are broadened beyond detection (65). In our holo-FBP sample, the ^{31}P resonance of Fe-bound phosphate also broadened beyond detection. Our data provide unambiguous compelling evidence that phosphate is the synergistic anion in recombinant FBP from *E. coli*. Our protein purification procedure does not involve any phosphate contamination, and ICP-AES data gave a 1:1:1 molar ratio of P/Fe/FBP in holo-FBP and 0:0:1 ratio in apo-FBP. After adding excess carbonate to holo-FBP solution to displace the bound phosphate, a ^{31}P NMR resonance for free phosphate was detected (Fig. 5*B*). These findings indicate that phosphate is present as an exogenous ligand, the synergistic anion, and are supported by our UV-visible and EXAFS data.

The pink color of native nFBP or that which develops when Fe(III) is added to the apo-nFBP solution is attributed to an intense charge-transfer absorption band at 481 nm. The similarity of the visible spectrum to those of transferrins (13) and metal-phenolate complexes (66) suggests that they arise from tyrosine-metal interactions and that the charge-transfer band must be derived from a ligand phenolate (π) → metal ($d\pi^*$) transition as in the case of transferrins (67). The molar extinction coefficient at 481 nm (ϵ_{481}) was determined to be 2440 $M^{-1}cm^{-1}$, a value close to that reported by Nowalk *et al.* (21) and comparable with half that of Fe_2-hTF (ϵ_{465} = 4950 $M^{-1}cm^{-1}$ (68)). The molar extinction coefficients at 280 nm for apo-nFBP and holo-nFBP were determined as ϵ_{280} = 44,200 for apo-nFBP and ϵ_{280} = 48,900 for holo-nFBP, approximately half of those for apo-hTF and holo-hTF (ϵ_{280} = 93,000 $M^{-1}cm^{-1}$ and 103,000 $M^{-1}cm^{-1}$, respectively (69)).

The wavelength of maximum absorption is affected by the

bound synergistic anion, varying from 450 to 481 nm from oxalate to phosphate. Different synergistic anions may affect the energy levels of Fe(III) and cause small changes in the Fe–O (Tyr) bond lengths (Table IV), leading to differences in the energy levels between the charge donor (Tyr) and acceptor (Fe(III)) and contributing to the LMCT bandshifts in UV-visible spectra. Besides phosphate, other anions such as carbonate, oxalate, NTA, and pyrophosphate can serve as synergistic anions for Fe(III) in nFBP. The failure of phosphate to act as a synergistic anion for transferrins is probably because of its tetrahedral structure that cannot provide the appropriate geometry for interactions in the specific metal-anion-transferrin complex, whereas smaller carboxylates can bind to the metal ion as bidentate anions, leaving no space for the binding of water (13). This could also contribute to the stronger binding of iron (compared with nFBP). nFBP can accommodate both phosphates and carboxylates as synergistic anions, probably because the iron-binding cleft in FBP is larger and nearer to the surface and, therefore, more solvent-accessible. Phosphate can provide more sites than carbonate for hydrogen bonding with the protein side chains in the cleft. This may contribute to the stronger binding compared with carbonate. The state of protonation of bound phosphate or carbonate is unknown. Sulfate and perchlorate, although isostructural with phosphate, fail to act as synergistic anions under the conditions we have tried. This may attributed to their weaker coordination properties and weaker hydrogen-bonding ability arising from the lower polarity of Cl–O and S–O bonds compared with P–O and C–O bonds.

A comparison of the models determined by EXAFS for Fe·PO_4·nFBP and Fe·CO_3·nFBP shows that a series of minor changes in Fe-ligand bond lengths and angles together with a significant difference in overall backscattering intensity (reflected in the Debye-Waller factors) are responsible for the markedly different spectra. Viewed simplistically, Debye-Waller factors are a measure of the thermal and static disorder with respect to the Fe(III) atom. As the spectra were collected at the same low temperature and having ruled out factors during data collection, this difference is probably because of a real difference in static disorder. The largest change in distance on changing the synergistic anion from phosphate to carbonate is the shortening of the Fe–O(Tyr-196) distance by 0.12 Å. The shorter distance for the carbonate complex can be directly equated with its larger extinction coefficient compared with the phosphate complex. The accuracy of metal-ligand bond lengths in protein x-ray crystal structures is notoriously difficult to assess unless diffraction data to atomic resolution (better than 1.2 Å) are available. Global estimates vary for lower resolution diffraction but range from ~0.1 to 0.15 Å for 1.5–2.0 Å diffraction data to ≥0.2 Å for >2 Å data (70). The x-ray structure of hFBP (9) was determined at 1.6 Å and nFBP as 2.2 Å, suggesting that bond length errors may be of the order of 0.1 and 0.2 Å, respectively. Thus, the differences observed between Fe-ligand bond lengths in the two crystal structures compared with the Fe-PO_4-nFBP EXAFS are mostly within the estimated errors for each crystal structure. It should be noted that the differences observed for three of the bond lengths in the hFBP (Glu-57, 0.13 Å; Tyr-195, 0.15 Å; Tyr-196, 0.16 Å) and one from the nFBP structure (Tyr-196, 0.20 Å) are at the top end of the range. The bond length errors from EXAFS do not have this same dependence and have been calculated to be in the range of <0.01–0.04 Å for liganding atoms in this study. Thus, this analysis is a good illustration of the complementarity of x-ray diffraction and EXAFS for metalloprotein studies. The crystal structure provides the metal site topology and (approximate) metal-ligand bond lengths, whereas EXAFS "fine tunes" these bond lengths to the equivalent of atomic resolution. As crystallographic data are not available for the CO_3 adduct, the EXAFS data are currently the only structural information on FBPs with an alternative biologically relevant synergistic anion bound.

Whereas EXAFS is capable of determining metal-atom distances with high accuracy, it is not able to measure other inter-atom distances to anywhere near this level with the exception of unusual cases (*e.g.* simple high symmetry systems with significant multiple scattering). Therefore, it is appropriate to consider the accuracy of the glutamate position and of the glutamate-water and glutamate-anion hydrogen bond lengths. The distances of the individual glutamate atoms to Fe are accurate to the normal level for an EXAFS analysis as direct Fe-atom distances have been determined. The geometry of the fragment has been preserved through the use of constrained (rigid body) and restrained refinement methods. However, the absolute position of the fragment with respect to the other ligands will have significantly greater uncertainty because assumptions had to be made regarding how to achieve the rotation. In placing the glutamate residue, it was assumed that there was no movement of the protein backbone, no change in any bond lengths within the glutamate, and that movement could arise only from an allowed rotation (around the CG–CD bond or CA–CB bond for the alternative rotamer) and a change in the bond angle between the ligand and the metal. Thus, the absolute position of the glutamate is chemically reasonable and is the best fit to the data. Comparisons of the three methods used to position Glu-57 and the crystallographic coordinates suggest an uncertainty in the absolute position of the glutamate with respect to the other ligands of approximately 0.7 Å. Because most of this is attributed to different angular orientations, the effect on the proposed hydrogen-bonding network is smaller than this. Hydrogen-bond lengths and angles are within acceptable values in all three models of the Fe·PO_4·nFBP data and also for the Fe·CO_3·nFBP data.

The difficulty in fitting the crystallographic coordinates to the EXAFS data and reliability of both the EXAFS data and fit have been extensively explored. Reference data collected at the same time show that the EXAFS data are reliable. Additionally, the 2.6 Å peak is present in two otherwise quite distinct data sets. The difficulty in fitting the 2.6 Å peak would not have been observed if only the first shell (using single scattering) had been fitted. Multiple scattering analysis is not new, but retaining the three-dimensional coordinates is a more recent innovation. However, this difficulty would still have been present without the three-dimensional information (*i.e.* if multiple scattering only within each ligand had been included). A large number of permutations of the structure was examined, but none involving the tyrosines, histidine, synergistic anion, or water ligands fitted the 2.6 Å peak. The use of constraints and restraints to maintain the internal geometry of the ligands significantly reduces the number of degrees of freedom of the model, thereby increasing the likelihood that a unique solution has been found. An examination of the calculated scattering pathways for the best EXAFS fit using the crystallographic Glu orientation (see Table III, Constrained Fit before rotation of Glu-57) suggests that the absence of calculated scattering at 2.6 Å is not the result of destructive (out of phase) scattering pathways. Two carbon/nitrogen/oxygen atoms were required to fit this peak. Although a fit could have been obtained by including an additional ligand(s) at this distance, there is no evidence to support such a model. However, this peak and the EXAFS data were readily modeled on changing the Glu position. The sensitivity of EXAFS data on this type of structure to the orientation of a carboxylate group is amply demonstrated

by the Fe·EHPG complex. The overall similarity of the Fe·PO_4·nFBP and Fe·CO_3·nFBP EXAFS models and the ease with which the CO_3 data were fitted after rotation of the Glu residue add credence to the veracity of the model. The changes to the crystallographic model required for Glu-57 involved an allowed rotation of a very flexible structure. Therefore, the EXAFS model is structurally allowed, chemically plausible, and is by far the best fit to the data. We cannot rule out the possibility that the difference in the position of the side chain of Glu-57 suggested by the EXAFS is a consequence of the difference in the data collection temperature between the EXAFS and the diffraction data. The EXAFS data were collected at 13 K, the nFBP diffraction data were collected at 100 K, and the hFBP diffraction data were collected at room temperature. The collection of protein diffraction data at 100 K has become routine in recent years, and there is a growing literature on the differences observed between protein structures at room temperature and at 100 K. Rotations of flexible side chains, especially of aspartate and glutamate, are fairly common. Collecting protein diffraction data at temperatures close to 13 K is still uncommon, and there is very little literature comparing observed structural differences at these temperatures. The orientation of the side chain of Glu-57 is the same in both crystal structures; therefore, the orientation proposed by EXAFS is not a result of the glass transition. However, we cannot rule out a structural/phase transition between 100 and 13 K (71). Other possible reasons for a real structural difference include pH and the method used to reconstitute the holo-protein. The pH value appears to be an improbable reason, because the pH of the EXAFS samples (pH 7.4) is close to that for the hFBP crystal structure (pH 6.6). A large excess of the synergistic anion was used when preparing the samples. It is conceivable that such a large excess displaced the conformational equilibrium away from the crystallographically observed conformer and toward the EXAFS-observed conformer. It may be possible that both the crystallographic and EXAFS-derived Glu orientations fit the crystallographic electron density maps. Such a scenario could arise if the electron density was not able to distinguish between the two orientations at the resolution available or if the electron density could represent a mixture of the two orientations with only one orientation modeled. Finally, it should be remembered that EXAFS is not readily able to distinguish mixtures. That the single orientation derived from EXAFS could be an average of the crystallographic orientation and some other undetermined orientation cannot be ruled not.

Because Ga(III), Bi(III), and Co(III) bind strongly to hTF, which is structurally homologous to nFBP, the weak binding of these metal ions to nFBP is surprising. There was competition between NTA and apo-FBP when $Ga(NTA)_2$ was used as a Ga source. Whether the binding constants are of the same order as those for metal-hydroxide binding, the binding may be greatly affected by the hydroxide concentration in the solution, *i.e.* pH. Taboy *et al.* (17) determined an effective binding constant for Fe(III) binding to nFBP of 2.4×10^{18} M^{-1} (pH 6.5) (298 K, 0.35 mM phosphate), which is within an order of magnitude of that for Fe(III) binding to the N-lobe of transferrin in the presence of carbonate. These differences may be attributed to the much greater solvent exposure and solvent accessibility of the iron site in FBP compared with transferrin.

CONCLUSION

We have prepared nFBP in high yield by cloning and overexpression of n*fbp* in *E. coli*. Our ICP-AES and ^{31}P NMR data suggest that phosphate is the native synergistic anion in recombinant nFBP from *E. coli*. Bound phosphate can be displaced by treating the holo-protein with excess bicarbonate, and EXAFS studies revealed marked changes in the local structure of Fe-PO_4-FBP compared with Fe·CO_3·FBP as a result of bond length and angle changes together with a significant difference in local ordering. EXAFS data allowed the refinement of the crystallographically determined metal-ligand bond lengths and suggested that the water, Glu, and monodentate synergistic anion are involved in an H-bonding network around the Fe site. The accurate structure of the Fe/anion site provides a reliable structural basis for rational design of novel chemotherapeutic agents targeted on this key protein, which is required for virulence and iron uptake in certain pathogenic bacteria. Oxalate, NTA, and pyrophosphate also appeared to be capable of serving as synergistic anions but not sulfate or perchlorate. Apo-FBP is much less stable than the holo-protein and binds only weakly to Ga(III) and Bi(III), unlike transferrin. Therefore, attempts to exploit the FBP route for periplasmic iron transport using heterometal ions, a possible strategy for the design of novel metalloantibiotics, will need to be based on other metals.

Acknowledgments—We thank Dr. R. Strange (Daresbury Laboratory) for the use of Fe-EHPG EXAFS data and Dr. H. Li (University of California, Irvine) for assistance with handling crystallographic data.

Note Added in Proof—Evidence for a phase change between 100 and 15 K has recently been reported for protein crystallographic data (71).

REFERENCES

1. Weinberg, E. D. (1997) *Perspect. Biol. Med.* **40**, 578–583
2. Posey, J. E., and Gherardini F. C. (2000) *Science* **288,** 1651–1653
3. Bullen, J., Rogers, H. J., and Griffiths, E., (1978) *Curr. Top. Microbiol. Immunol.* **80,** 1–35
4. Braun, V., and Killmann, H. (1999) *Trends. Biol. Sci.* **24**, 104–109
5. Aisen, P., Wessling-Resnick, W., and Leibold, E. A. (1999) *Curr. Opin. Chem. Biol.* **3,** 200–206
6. Ferreirós, C. M., Criado, M. T., and Gómez, J. A. (1999) *Comp. Biochem. Physiol.* **123,** 1–7
7. Meitzner, T. A., Tencza, S. B., Adhikari, P., Vaughan, K. G., and Nowalk, A. J. (1998) *Curr. Top. Microbiol. Immunol.* **225,** 113–135
8. Morse, S. A., Chen, C.-Y., LeFaou, A., and Meitzner, T. A. (1988) *Rev. Infect. Dis.* **10,** S306–S310
9. Bruns, C. M., Nowalk, A. J., Arvai, A. S., McTigue, M. A., Vaughan, K. G., Mietzner, T. A., and McRee, D. E. (1997) *Nat. Struct. Biol.* **4,** 919–924
10. Schryvers, A. B., and Stojiljkovic, I. (1999) *Mol. Microbiol.* **32,** 1117–1123
11. Tettelin, H., Saunder, N. J., Heidelberg, J., *et al.* (2000) *Science* **287,** 1809–1815
12. Parkhill, J., Achtman, M., James, K. D., *et al.* (2000) *Nature* **404,** 502–506
13. Baker, E. N. (1994) *Adv. Inorg. Chem.* **41,** 389–463
14. Bates, G. W., and Schlabach, M. R. (1975) *J. Biol. Chem.* **25,** 2177–2181
15. MacGillivray, R. T. A., Moore, S. A., Chen, J., Anderson, B. F., Baker, H., Luo, Y., Bewley, M. C., Smith, C. A., Murphy, M. E. P., Wang, Y., Mason, A. B., Woodworth, R. C., Brayer, G. D., and Baker, E. N. (1998) *Biochemistry* **37,** 7919–7928
16. Jeffrey, P. D., Bewley, M. C., MacGillivray, R. T. A., Mason, A. B., Woodworth, R. C., and Baker, E. N. (1998) *Biochemistry* **37,** 13978–13986
17. Taboy, C. H., Vaughan, K. G., Mietzner, T. A., Aisen, P., and Crumbliss, A. L. (2001) *J. Biol. Chem.* **276,** 2719–2724
18. Mietzner, T. A., Bolan, G., Schoolnik, G. K., and Morse, S. A. (1987) *J. Exp. Med.* **165,** 1041–1057
19. Berish, S. A., Mietzner, T. A., Mayer, L. W., Genco, C. W., Holloway, B. P., and Morse, S. A. (1990) *J. Exp. Med.* **171,** 1535–1546
20. Berish, S. A., Chen, C.-Y., Mietzner, T. A., and Morse, S. A. (1992) *Mol. Microbiol.* **6,** 2607–2615
21. Nowalk, A. J., Tencza, B. T., and Meitzner, T. A. (1994) *Biochemistry* **33,** 12769–12775
22. Hasnain, S. S., and Strange, R. W. (1990) in *Biophysics and Synchrotron Radiation* (Hasnain, ed) p. 104, Ellis Horwood Ltd., Chichester, United Kingdom
23. Binstead, N., Strange, R. W., and Hasnain, S. S. (1992) *Biochemistry* **31,** 12117–12125
24. Ellis, P. J., and Freeman, H. C. (1995) *J. Synchrotron Radiat.* **2,** 190–195
25. Fonda, E., Michalowicz, A., Randaccio, L., Tauzher, G., and Vlaic, G. (2001) *Eur. J. Inorg. Chem.* 1269–1278
26. Blackburn, N. J., Hasnain, S. S., Pettingill, T. M., and Strange, R. W. (1991) *J. Biol. Chem.* **266,** 23120–23127
27. Grossman, J. G., Crawley, J. B., Strange, R. W., Patel, K. J., Murphy, L. M., Neu, M., Evans, R. W., and Hasnain, S. S. (1998) *J. Mol. Biol.* **279,** 461–472
28. Cheng, M. C., Rich, A. M., Armstrong, R. S., Ellis, P. J., and Lay P. A. (1999) *Inorg. Chem.* **38,** 5703–5708
29. Nakajima, H., Honma, Y., Tawara, T., Kato, T., Park, S.-Y., Miyatake, H., Shiro, Y., and Aono, S. (2001) *J. Biol. Chem.* **276,** 7055–7061
30. Rehr, J. J. (1993) *Jpn. J. Appl. Phys.* pp. 32–40
31. Binsted, N., and Hasnain, S. S. (1996) *J. Synchrotron Radiat.* **3,** 185–196
32. Binsted, N. (1998) *EXCURV98: CCLRC Daresbury Laboratory Computer Program*, Warrington, United Kingdom
33. Cheung, K. C., Strange, R. W., and Hasnain, S. S. (2000) *Acta Crystallogr. Sec.*

D **56,** 697–704
34. Bauer, H. F., and Drinkard, W. C. (1960) *J. Am. Chem. Soc.* **82,** 5031–5032
35. Bauer, H. F., and Drinkard, W. C. (1966) *Inorg. Syn.* **8,** 202–204
36. He, Q. Y., Mason, A. B., and Woodworth, R. C. (1996) *Biochem. J.* **318,** 145–148
37. Smith, P. K., Krohn, R. I., Hermanson, G. T., Mallia, A. K., Gartner, F. H., Provenzano, M. D., Fujimoto, E. K., Goeke, N. M., Olson, B. J., and Klenk. D. C. (1985) *Anal. Biochem.* **150,** 76–85
38. Bax, A., Griffey, R. H., and Hawkins, B. L. (1983) *J. Magn. Reson.* **55,** 301–315
39. Shaka, A. J., Barker, P. B., and Freeman, R. (1985) *J. Magn. Reson.* **64,** 547–552
40. Ellis, P. (1995) *Studies of Metalloproteins Using EXAFS and XRD*, Ph.D. thesis, University of Sydney, Sydney, Australia
41. Rehr, J. J., and Albers, R. C. (1990) *Physiol. Rev.* **41,** 8139–8149
42. Hedin, L., and Lundquist, S. (1969) *Solid State Phys.* **23,** 1–181
43. Rehr, J. J., de Leon. J., Zabinsky, S. I., and Albers, R. C. (1991) *J. Am. Chem. Soc.* **113,** 5135–5140
44. Koenig, D. F. (1965) *Acta Crystallogr.* **18,** 663–673
45. Bailey, N. A., Cummins, D., Mckenzie, E. D., and Worthington, J. M. (1981) *Inorg. Chim. Acta* **50,** 111–120
46. Strange, R. W., Reinhammer, B., Murphy, L. M., and Hasnain, S. S. (1995) *Biochemistry* **34,** 220–231
47. Engh, R. A., and Huber, R. (1991) *Acta Crystallogr. Sec. A* **47,** 392–400
48. Report of the International XAFS Society Standards and Criteria Committee (2000) *Error Reporting Recommendations* (Sayers, D., Chair) website: ixs.csrri.iit.edu
49. Bertini, I., Luchinat, C., and Aimes, S. (1996) *Coord. Chem. Rev.* **150,** 1–292
50. Guo, M. (2000) *Proteins and Nucleic Acids as Targets for Titanium(IV)*, Ph.D. thesis, University of Edinburgh, Edinburgh, United Kingdom
51. Bali, P. K., Harris, W. R., and Nesset-Tollefson, D. (1991) *Inorg. Chem.* **30,** 502–508
52. Schlabach, M. R., and Bates, G. W. (1975) *J. Biol. Chem.* **250,** 2182–2188
53. Mizutani, K., Yamashita, H., Kurokawa, H., Mikami, B., and Hirose, M. (1999) *J. Biol. Chem.* **274**, 10190–10194
54. Kojima, N., and Bates, G. W. (1981) *J. Biol. Chem.* **256,** 12034–12039
55. Harris, W. R., and Pecoraro, V. L. (1983) *Biochemistry* **22,** 292–299
56. Guo, M. L., Sun, H., McArdle, H. J., Gambling, L., and Sadler, P. J. (2000) *Biochemistry* **39,** 10023–10033
57. Guo, M. L., and Sadler, P. J. (2000) *J. Chem. Soc. Dalton Trans.* pp. 7–9
58. McRee, D. E. (1992) *J. Mol. Graph.* **10,** 44–46
59. Pecoraro, V. L., Harris, W. R., Carrano, C. J., and Raymond, K. N. (1981) *Biochemistry* **20,** 7033–7039
60. Patch, M. G., Simolo, K. P., and Carrano, C. J. (1983) *Inorg. Chem.* **22,** 2630–2634
61. Harris, D. C., and Aisen, P. (1989) in *Iron Carriers and Iron Proteins* (Loehr, T. M., ed) pp. 239–351, VCH Publishers, Inc., New York
62. Harris, W. R. (1986) *Biochemistry* **25**, 803–808
63. Sun, H., Li, H., and Sadler, P. J. (1999) *Chem. Rev.* **99,** 2817–2842
64. Bruns, C. M., Anderson, D. S., Vaughan, K. G., Williams, P. A., Nowalk, A. J., McRee, D. E., and Mietzner, T. A. (2001) *Biochemistry*, **40,** 15631–15637
65. Zweier, J. L., Wooten, J. B., and Cohen, J. S. (1981) *Biochemistry*, **20,** 3505–3510
66. Gaber, B. P., Miskowski, V., and Spiro, T. G. (1974) *J. Am. Chem. Soc.* **96,** 6868–6873
67. Patch, M. G., and Carrano, C. J. (1981) *Inorg. Chim. Acta* **56,** L71–L73
68. Bali, P. K., and Harris, W. R. (1990) *Arch. Biochem. Biophys.* **281**, 251–256
69. Chasteen, N. D., White, L. K., and Campbell, R. F. (1977) *Biochemistry* **16,** 363–368
70. Cruikshank, D. W. J. (1996) *CCP4 Proceedings:DL-CONF-960–001* (Dodson, E., ed) pp. 11–23, Warrington, United Kingdom
71. Hanson, B. L., Harp, J. M., Kirschbaum, K., Schall, C. A., DeWitt, K., and Howard, A. (2002) *J. Synchrotron Radiat.* **9,** 375–381